Title

Creation of two-dimensional layered Zintl phase by dimensional manipulation of crystal structure.

Journal

Science Advances, 5(6)

Authors

Song, Junseong

Song, Hyun

Wang, Zhen

et al.

Publication Date

2019-06-01

DOI

10.1126/sciadv.aax0390

Peer reviewed

MATERIALS SCIENCE

Creation of two-dimensional layered Zintl phase by dimensional manipulation of crystal structure

Junseong Song[1], Hyun Yong Song[1,2], Zhen Wang[1], Seokhee Lee[1,3], Jae-Yeol Hwang[1,4], Seung Youb Lee[5], Jouhahn Lee[5], Dongwook Kim[6], Kyu Hyong Lee[7], Youngkuk Kim[6], Sang Ho Oh[1], Sung Wng Kim[1,2]*

The discovery of new families, beyond graphene, of two-dimensional (2D) layered materials has always attracted great attention. However, it has been challenging to artificially develop layered materials with honeycomb atomic lattice structure composed of multicomponents such as hexagonal boron nitride. Here, through the dimensional manipulation of a crystal structure from sp^3-hybridized 3D-ZnSb, we create an unprecedented layered structure of Zintl phase, which is constructed by the staking of sp^2-hybridized honeycomb ZnSb layers. Using structural analysis combined with theoretical calculation, it is found that the 2D-ZnSb has a stable and robust layered structure. The bidimensional polymorphism is a previously unobserved phenomenon at ambient pressure in Zintl families and can be a common feature of transition metal pnictides. This dimensional manipulation of a crystal structure thus provides a rational design strategy to search for new 2D layered materials in various compounds, enabling unlimited expansion of 2D libraries and corresponding physical properties.

INTRODUCTION

The advent of Dirac physics of graphene has triggered an explosive increase in the research of two-dimensional (2D) materials, which are of great interest in diverse fields ranging from electronics, magnetics, energy, and chemistry to quantum physics (*1*–*7*). However, except for elemental 2D atomic crystals such as silicone (*8*), most of the present 2D researches have been focused on only a few 2D materials that can be exfoliated into a single or several atomic layers from their mother compounds with an inherent 2D layered structure (*1*–*5*, *7*, *9*). This largely restricted methodologies for the synthesis of 2D materials to two approaches: exfoliation and chemical vapor deposition (*1*–*9*). To expand the research of 2D materials while ensuring the diversity in chemical compositions and properties, it is highly desirable that a new 2D material can be artificially created by a novel synthetic approach applicable to a variety of material groups.

In the context of a new material discovery, the transformation of a crystal structure has been widely recognized as a key factor (*10*, *11*). The temperature-, pressure-, and electrostatic doping–induced structural phase transitions have been a core subject for exploring a novel crystal structure and switching material properties of 2D materials (*12*–*14*). In particular, most transition metal dichalcogenides exhibit the polymorphic phase transition that opens up access to diverse properties, including superconducting and topological states (*15*). This transition also leads to promising applications such as electronic homojunction and photonic memory devices, as well as catalytic energy materials (*16*–*18*). However, these polymorphic transitions only occurred between different layered structures in the same two dimensions and have not yet been realized between different dimensionalities of a crystal structure at ambient pressure. Reaching an ultimate crystal engineering that can alter the structural dimensionality of multicomponent compounds is promising to be a next frontier in material science beyond the allotropes of carbon. Here, we establish the bidimensional polymorphism through the discovery of a 2D layered structure in Zintl phases that have a vast number of chemical compositions with p-block metals satisfying the valence electron count rule (*19*). By considering the sp^2 hybrid orbital bonding of honeycomb-structured 2D atomic crystals such as graphene and hexagonal boron nitride, one may expect that 3D structured Zintl phases with sp^3 hybrid orbital bonding transform to the sp^2 honeycomb-structured 2D layered materials via electron transfer (*19*, *20*). As a proof-of-concept material, we have selected a 3D orthorhombic ZnSb (3D-ZnSb) Zintl phase and created the unprecedented 2D layered structure of ZnSb (2D-ZnSb).

RESULTS

Creation of 2D layered ZnSb

Our methodological strategy to create the 2D-ZnSb Zintl phase is schematically illustrated in Fig. 1A. First, we aimed to synthesize layered AZnSb (2D-AZnSb) ternary compounds (A refers to alkali metal, and here, we present 2D-LiZnSb as a representative form; see also fig. S1 for A = Na and K) that can have a layered structure of ZnSb from the transformation of 3D-ZnSb by A alloying, although each 3D-ZnSb and 2D-AZnSb phase can be synthesized independently (*21*, *22*). Then, the selective etching of A ions from 2D-AZnSb has been performed to create the 2D-ZnSb via two different processes: (i) chemical reaction in deionized (DI) water–incorporated solutions and (ii) electrochemical ion etching reaction in alkali-based electrolyte. We successfully synthesized the polycrystalline and single crystalline 2D-LiZnSb by Li alloying into the polycrystalline 3D-ZnSb (Fig. 1B; see also fig. S1 for other synthetic routes of 2D-LiZnSb). For the etching of Li ions, we exclusively used the 2D-LiZnSb single crystals to further demonstrate the feasibility of exfoliation into large-scale nanosheets as a 2D material. Notably, all Li-etched crystals showed that only one broad x-ray diffraction (XRD) peak appeared at approximately 29.8° (Fig. 1C), which is analogous to XRD patterns for intercalated graphite and other 2D materials (*23*–*25*). Furthermore, we observed cracks along

[1]Department of Energy Science, Sungkyunkwan University, Suwon 16419, Republic of Korea. [2]Center for Integrated Nanostructure Physics, Institute for Basic Science, Suwon 16419, Republic of Korea. [3]Energy & Enviroment Division, Korea Institute of Ceramic Engineering and Technology (KICET), Jinju 52851, Republic of Korea. [4]Department of Physics, Pukyong National University, Busan 48513, Republic of Korea. [5]Advanced Nano Surface Research Group, Korea Basic Science Institute, Daejeon 34133, Republic of Korea. [6]Department of Physics, Sungkyunkwan University, Suwon 16419, Republic of Korea. [7]Department of Materials Science and Engineering, Yonsei University, Seoul 03722, Republic of Korea.
*Corresponding author. Email: kimsungwng@skku.edu

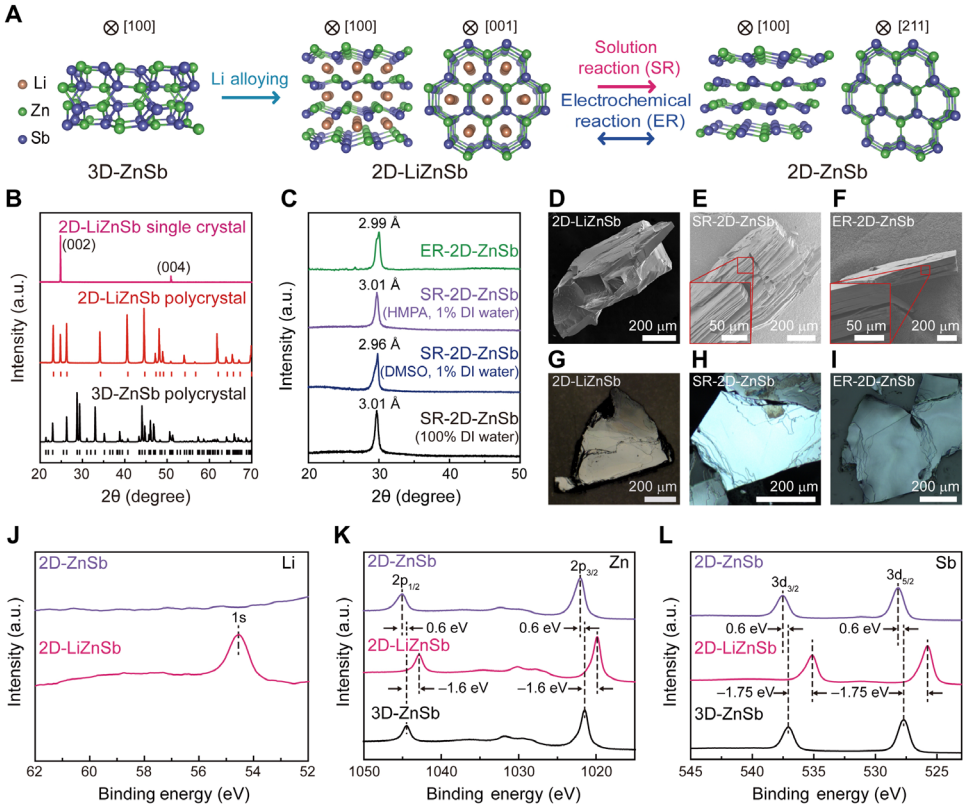

Fig. 1. Creation of 2D layered ZnSb. (**A**) Schematic illustration of the dimensional manipulation of a crystal structure from 3D-ZnSb to 2D-ZnSb via Li alloying and etching processes. The Li alloying into 3D-ZnSb was conducted by thermal and electrochemical reactions (ERs) (see Materials and Methods and fig. S1). The selective etching of Li ions was conducted by reacting with polar solvent solution reaction (SR). A reversible process of alloying and etching occurs in the mean of electrochemical reaction (ER). (**B**) XRD patterns of 3D-ZnSb and 2D-LiZnSb. The 2D-LiZnSb polycrystal and single crystal were synthesized by using the synthesized 3D-ZnSb as a precursor. All patterns are well matched with the simulated patterns of corresponding compounds. a.u., arbitrary units. (**C**) XRD patterns of 2D-ZnSb crystals obtained by solution reaction and electrochemical reaction processes. For the solution reaction process, water-based solutions [DI water and dimethyl sulfoxide (DMSO) with 1 volume % of DI water, and hexamethyl phosphoric triamide (HMPA) with 1 volume % of DI water] were used. For the electrochemical reaction process, 1 M $LiPF_6$ dissolved in 1:1 mixture of ethylene carbonate and diethyl carbonate solution was used as an electrolyte. The interlayer distances were calculated from the angle of highest intensity. (**D** to **I**) Scanning electron microscopy (D to F) and optical images (G to I) of 2D-LiZnSb and 2D-ZnSb created by the solution reaction and electrochemical reaction processes (see also fig. S2 for Na- and K-etched samples). The flakes of 2D-ZnSb were exfoliated by mechanical cleaving using 3M tape. The exfoliated nanosheets obtained from the solution reaction and ultrasonication processes are shown in fig. S4. (**J** to **L**) X-ray photoelectron spectroscopy (XPS) spectra of Li 1s (J), Zn 2p (K), and Sb 3d (L) for 3D-ZnSb, 2D-LiZnSb, and 2D-ZnSb, respectively. The Li 1s peak (54.6 eV) of 2D-LiZnSb indicates the Li^{1+} state. While the binding energies of the Zn $2p_{3/2}$ (1019.8 eV) and Sb $3d_{5/2}$ (525.8 eV) are significantly lower than the Zn $2p_{3/2}$ (1021.5 eV) and Sb $3d_{5/2}$ (527.6 eV) in 3D-ZnSb, the binding energies of Zn $2p_{3/2}$ (1022.1 eV) and Sb $3d_{5/2}$ (528.2 eV) of 2D-ZnSb are slightly higher than those of 3D-ZnSb.

the planar direction in all Li-etched crystals (Fig. 1, E and F; see also fig. S2 for A-etched crystals), providing qualitative similarities to other 2D materials (*4*, *23*–*25*). The inductively coupled plasma mass spectroscopy (ICP-MS) measurements for the etched crystals that show no lithium content, maintaining the chemical ratio of 1:1 for Zn and Sb (fig. S3U), support the observation that the Li ion etching completes the formation of a 2D-ZnSb crystal. The Li-etched 2D-ZnSb crystals were easily cleaved by an adhesive tape exfoliation technique, exhibiting a typical flat surface as reported 2D materials (Fig. 1, H and I) (*26*). It should be noted that the 2D-ZnSb is stable in an air atmosphere without structural degradation. In addition, the 2D-ZnSb showed the same optical image as that in Fig. 1H after soaking in DI water over a day.

To understand the role of Li alloying and etching on the structural transformations, we examined the x-ray photoelectron spectroscopy (XPS) measurements that reveal the difference between the chemical bonding nature between 3D and 2D crystals (Fig. 1, J to L). From the binding energies for the Zn_{2p} and Sb_{3d} of 3D-ZnSb with additional Sb-Sb bonding (*27*), a large negative shift was observed for both Zn_{2p} and Sb_{3d} of 2D-LiZnSb. This change signifies that a substantial electron doping occurs for Zn-Sb and Sb-Sb bondings of 3D-ZnSb, forming the puckered honeycomb ZnSb lattice in 2D-LiZnSb that has a different hybridized bonding state from 3D-ZnSb. Because the 2D-LiZnSb is a Zintl phase constructed by a Li^{1+} ion and a polyanionic $[ZnSb]^{-1}$ layer (*28*), the transferred electrons are accommodated in the hexagonal Zn-Sb bonding without additional Sb-Sb bonding of 3D-ZnSb. On the other hand, the positive shift of Zn_{2p} and Sb_{3d} in 2D-ZnSb from those in 3D-ZnSb and 2D-LiZnSb led us to hypothesize two possibilities: (i) a removal of doped electrons when Li cations are etched, turning back to similar bonding characters of 3D-ZnSb, or (ii) a generation of new Zn-Sb bonding network different from both 3D-ZnSb and 2D-LiZnSb. However, the former can be excluded because there is no trace of 3D-ZnSb in the XRD patterns and transmission electron microscopy (TEM) observations. For the latter, we used scanning tunneling electron microscopy (STEM) combined

with energy-dispersive spectroscopy (EDS) elemental mapping to directly confirm the atomic structure of 2D-ZnSb.

Crystal structure of 2D layered ZnSb

Compared to the 2D-LiZnSb with puckered honeycomb ZnSb lattice in the stacking order of A(ZnSb)-Li-B(ZnSb)-Li-A(ZnSb)-Li-B(ZnSb) (Fig. 2, A to C), the 2D-ZnSb has the same puckered honeycomb ZnSb lattice [the top view along the (211) direction; Fig. 2, D to F] but has a different stacking structure with an overturned ZnSb layer (B → B′) in the order of A(ZnSb)-B′(ZnSb)-A(ZnSb)-B′(ZnSb) (Fig. 2E). Furthermore, the slanted layer stacking in the order of A-B′-A-B′ makes the two different interlayer distances, facing with Zn-Zn (2.64 Å between

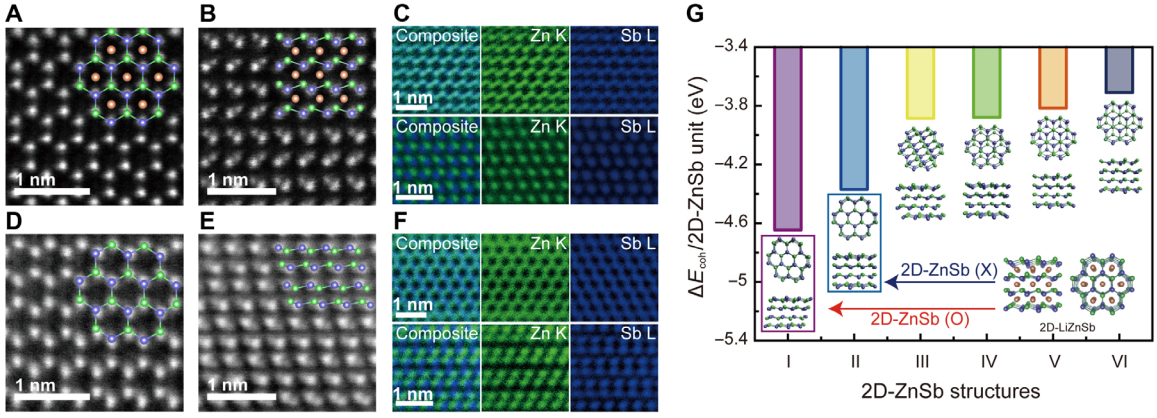

Fig. 2. Crystal structure of 2D layered ZnSb. (**A** and **B**) Atomic resolution STEM-HAADF (high-angle annular dark-field) images of 2D-LiZnSb along the [110] (A) and [001] (B) zone axes, respectively. (**C**) Atomic resolution STEM-EDS elemental mapping for 2D-LiZnSb along the [110] (top) and [001] (bottom) zone axes. (**D** and **E**) Atomic resolution STEM-HAADF images of 2D-ZnSb along the [110] (D) and [211] (E) zone axes. The determined crystal structure of 2D-ZnSb, together with the results in fig. S5, is visualized in fig. S6, where the detailed structural parameters are listed. The atomic distances of 2D-ZnSb are compared with those of 3D-ZnSb and 2D-LiZnSb, as shown in fig. S6. From the observation at [211] zone axis of 2D-ZnSb, the honeycomb lattice is slightly tilted, as explained in fig. S6. (**F**) Atomic resolution STEM-EDS elemental mapping for 2D-ZnSb along the [110] (top) and [211] (bottom) zone axes. For the detection of lithium, the STEM–EELS (electron energy-loss spectroscopy) technique was used, showing the clear existence and absence of lithium in 2D-LiZnSb and 2D-ZnSb, respectively, as shown in fig. S3. (**G**) Cohesive energy (ΔE_{coh}) calculation of predictable 2D-ZnSb structures. Structure I that is determined from the STEM observations exhibits the lowest energy compared with other candidates, showing excellent agreement between experiments and calculations.

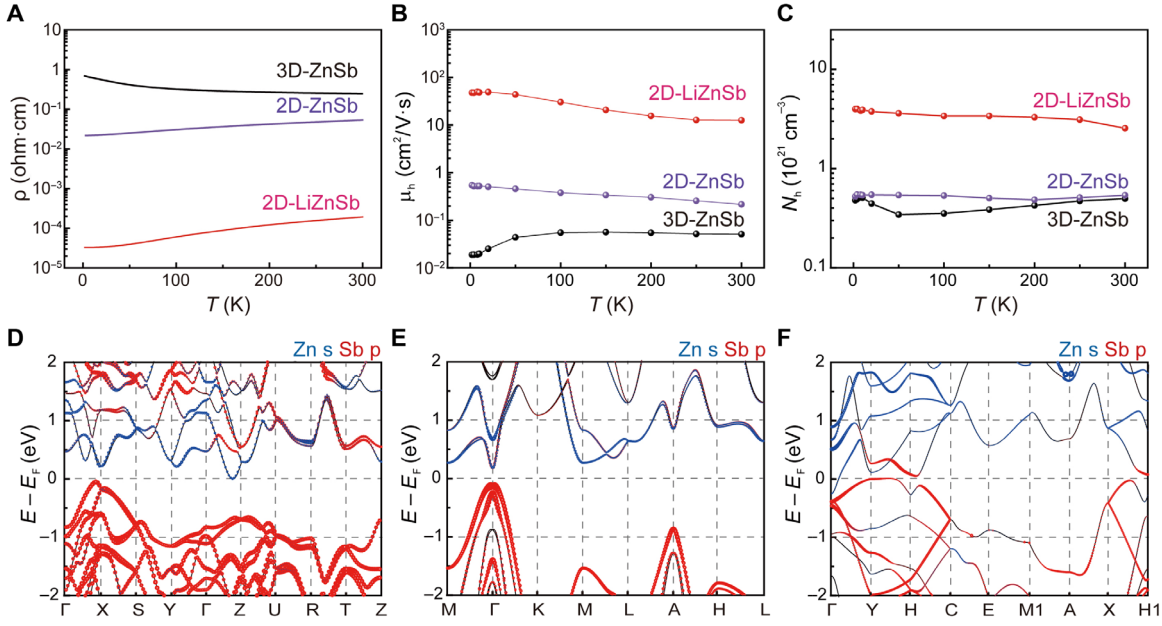

Fig. 3. Electronic properties of 2D layered ZnSb. (**A** to **C**) Temperature dependence of electrical resistivity (A), Hall mobility (B), and carrier concentration (C) for 3D-ZnSb, 2D-LiZnSb, and 2D-ZnSb. The bidimensional polymorphs of 3D-ZnSb and 2D-ZnSb show the metal-insulator transition. (**D** to **F**) Electronic band structures of 3D-ZnSb (D), 2D-LiZnSb (E), and 2D-ZnSb (F). The density of states for 3D-ZnSb, 2D-LiZnSb, and 2D-ZnSb are shown in fig. S9. The band structures of 3D-ZnSb (D) and 2D-LiZnSb (E) indicate that both are semiconductors with a well-defined indirect bandgap of 0.05 and 0.29 eV, respectively. A low electrical resistivity and a high carrier concentration of 2D-LiZnSb indicate a heavily doped semiconducting behavior.

B′ and A) and Sb-Sb (2.91 Å between A and B′). These stretched interlayer distances between both Zn-Zn and Sb-Sb atoms are interpreted as weak interlayer bondings, verifying that the 2D-ZnSb is an exfoliatable layered material (figs. S6 and S7). This weak interlayer interaction in 2D-ZnSb implies that the $[ZnSb]^{-1}$ layer skeleton of 2D-LiZnSb is energetically unfavorable itself and thus it stabilized by the ionic bonding with Li^{1+} ions in 2D-LiZnSb, separating each $[ZnSb]^{-1}$ layer by the distance of 2.76 Å (Zn-Sb bonding length in out-of-plane direction). Therefore, the $[ZnSb]^{-1}$ layer skeleton in the 2D-ZnSb is stabilized by the weakly interfaced Zn-Zn and Sb-Sb interactions. It is also confirmed from the ab initio cohesive energy calculations that the observed layered structure is the most stable (pink bar) among the predictable layered structures for 2D-ZnSb (Fig. 2G), although one may expect that the ZnSb layer skeleton of 2D-LiZnSb remains as it is (blue bar) when Li cations are etched. On the other hand, the newly evolved layered structure of 2D-ZnSb completes the first discovery of the bidimensional polymorphism in Zintl phases at ambient pressure, where the sp^3-hybridized bonding state in 3D-ZnSb was manipulated into the sp^2 state in 2D-ZnSb honeycomb lattice, validating the octet rule for Zintl concept (see further details in fig. S8). In previous studies of Zintl phases, bidimensional polymorphic transitions between 3D and 2D structures have been only observed under high pressure (*29*, *30*). The present bidimensional polymorphism between 3D-ZnSb and 2D-ZnSb thus emphasizes the potential and broad availability of such an electron transfer that manipulates a hybridized bonding state, transforming the crystal structure even in a bulk scale.

Electronic properties of 2D layered ZnSb

We examined the electrical transport properties of bidimensional ZnSb polymorphs and 2D-LiZnSb crystals, together with first-principles calculations of their electronic energy band structures (Fig. 3). Contrary to the semiconducting 3D-ZnSb, both 2D-LiZnSb and 2D-ZnSb exhibit the metallic conduction behavior (Fig. 3A). The electrical mobilities of both 2D-LiZnSb and 2D-ZnSb increase with the decrease in temperature, showing a higher value than that of 3D-ZnSb (Fig. 3B). The band structures of 3D-ZnSb and 2D-LiZnSb (Fig. 3, D and E) exhibit a semiconducting character with a well-defined indirect bandgap of 0.05 and 0.29 eV, respectively. From the metallic conduction of 2D-LiZnSb, one would expect for a heavily doped semiconductor that is coincident with the reported experimental results (*22*). In contrast, the band structure of 2D-ZnSb (Fig. 3F) exhibits a semimetallic character with the overlapping of conduction and valence bands at the Fermi level. Considering

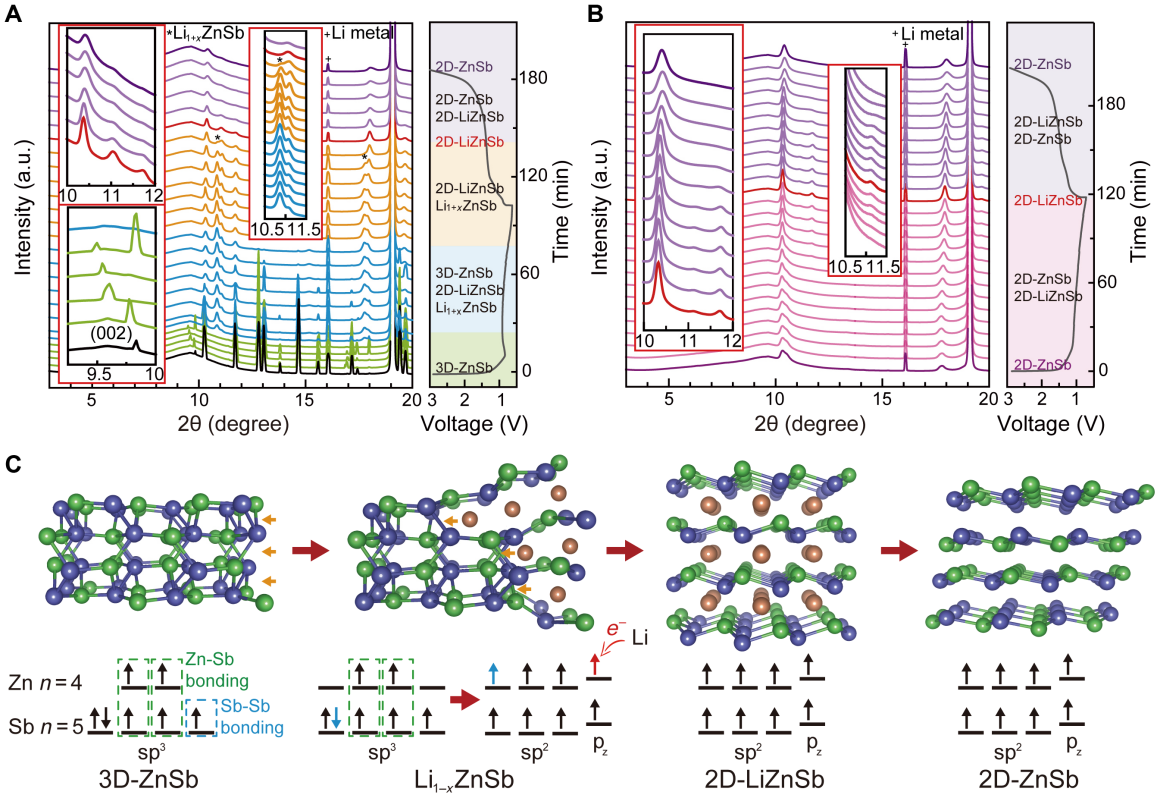

Fig. 4. Dimensional manipulation of a crystal structure for the bidimensional polymorphic ZnSb. (**A** and **B**) In situ synchrotron powder XRD patterns using 3D-ZnSb (A) and 2D-ZnSb (B) via the electrochemical reaction. The alloying and etching processes were controlled by reducing and increasing voltage potential, respectively. The inset (bottom left) of (A) shows the peak shift of (002) plane for 3D-ZnSb. The inset (top left) of (A) shows the disappearance of diffraction peaks' corresponding (002) and (101) planes at 11.1° and 11.7° of 2D-LiZnSb with Li etching, indicating the transformation to 2D-ZnSb. The inset (middle) shows the appearance and disappearance of $Li_{1+x}ZnSb$ by-product with discharging and charging reactions, respectively. The insets of (B) show the same changes observed in the insets (top left and middle) of (A). No diffraction peaks of 3D-ZnSb were observed during the reversible structural transformation by Li alloying and etching processes. The detailed evolution and degradation of diffraction peaks during the transformation are shown in fig. S10. (**C**) Schematic illustration of the dimensional manipulation of a crystal structure, along with the transition of hybridized bonding characters from sp^3 of 3D-ZnSb to sp^2 of 2D-LiZnSb and 2D-ZnSb. The displacement of the blue arrow in Sb fifth to Zn fourth orbital depicts the covalent bonding character between Zn and Sb in the honeycomb lattice. The electron transfer from Li to sp^3-hybridized state of 3D-ZnSb enables the transition to sp^2-hybridized state of honeycomb ZnSb lattice in 2D-LiZnSb and 2D-ZnSb.

the band widths of Zn s and Sb p bands, we attribute the transport properties of 2D-LiZnSb and 2D-ZnSb to the enhanced hopping of electrons along the in-plane directions, which originates from the change in bonding character between Zn and Sb from sp^3 of 3D-ZnSb to sp^2 bonding of a puckered honeycomb lattice in 2D-LiZnSb and 2D-ZnSb, showing good agreement with the enhanced mobility of 2D-LiZnSb and 2D-ZnSb than that of 3D-ZnSb, as shown in Fig. 3B. This result can be understood from the anisotropy in the energy band structures of 2D-LiZnSb and 2D-ZnSb, showing the prominent band evolutions in the in-plane M-Γ-K direction for 2D-LiZnSb and Γ-Y-H-C direction for 2D-ZnSb, respectively. Furthermore, comparing the band dispersions of 2D-LiZnSb and 2D-ZnSb, the larger curvature in the valley of conduction and valence band in the in-plane direction of 2D-LiZnSb can explain the higher mobility than that of 2D-ZnSb. Each ZnSb layer is separated by a Li cationic layer in 2D-LiZnSb, but ZnSb layers in 2D-ZnSb are interacted weakly with the interfaced Zn-Zn and Sb-Sb interactions. Notably, the enlarged band widths of Zn s and Sb p bands for 2D-ZnSb are ascribed to the enhanced sp^2 nature of honeycomb-structured layers with weakened interlayer interactions, resulting in the semimetal band structure with the electron and the hole pockets forming in different regions of the Brillouin zone. Furthermore, from the theoretical calculation, we confirmed that the 2D-ZnSb can be exfoliated into the bilayer, which exists in an energetically stable form as a 2D material (fig. S7). It is, however, noted that the monolayer 2D-ZnSb is energetically unfavorable.

Dimensional manipulation of crystal structure for the bidimensional polymorphic ZnSb

Last, to demonstrate how the structural transformation occurs for bidimensional ZnSb polymorphs via the formation of 2D-LiZnSb, we examined in situ synchrotron powder XRD during the electrochemical reaction (Fig. 4). When the potential voltage is decreased down to 1.0 V for 3D-ZnSb (black), the only (002) peak of 3D-ZnSb at 9.8° starts to shift to lower angle, indicating the increase in distance (002) plane (green). As the electrochemical reaction for Li alloying proceeds, the peaks of 3D-ZnSb lose the intensity and the peaks of 2D-LiZnSb appear at 11.1° and 18.0° (azure), together with a shoulder (marked with asterisks), which comes from $Li_{1+x}ZnSb$ (*31*), and then a pure 2D-LiZnSb is formed (red) after the complete disappearance of 3D-ZnSb and $Li_{1+x}ZnSb$ (ocher). As the Li cations are extracted by increasing potential voltage, the peaks at 11.1° and 11.7° (also 18.0° small shift to higher angle when forming 2D-ZnSb) of 2D-LiZnSb fade away (lilac), finally transforming to the 2D-ZnSb (purple). This transformation is schematically illustrated in Fig. 4C, showing that the Li atoms selectively penetrate into the 3D-ZnSb along the (00*l*) plane pointed by orange arrows, breaking the Zn-Sb and Sb-Sb bodings. Simultaneously, the transferred electrons change the hybridized bonding state from sp^3 in 3D-ZnSb to sp^2 of the $[ZnSb]^{-1}$ layer in 2D-LiZnSb, forming a puckered honeycomb lattice. We noted that, when the transformation is finished by removing Li cations from 2D-LiZnSb, the 2D-ZnSb is evolved, not turning to the 3D-ZnSb. Moreover, it is revealed that the newly evolved Zn-Sb honeycomb structure in the layered 2D-ZnSb crystal is robust. Using the 2D-ZnSb obtained from solution reactions as starting materials (Fig. 1, C, E, and H), we have observed a reversible transformation, which only occurs between 2D-LiZnSb and 2D-ZnSb. As shown in Fig. 4B, the peaks at 11.1° and 11.7° of 2D-LiZnSb appear and disappear repeatedly, indicating an exclusive transformation between 2D-LiZnSb and 2D-ZnSb without turning to 3D-ZnSb. These results indicate that the layered 2D-ZnSb, once formed, is a stable material with a puckered honeycomb structure, validating a stable bidimensional polymorphic transition and anticipating an application for sustainable alkali-ion batteries.

DISCUSSION

In summary, our rigorous experimental and theoretical studies demonstrate that 2D layered Zintl phases can be created by the manipulation of a structural dimensionality. This methodology establishes the first bidimensional polymorphic family in Zintl phases at ambient pressure, enabling the use of new phase transformations as a general synthesis route. Last, this work provides a rational design strategy for exploring new 2D layered materials and potentially unlocking further properties of interest such as 2D magnetism, ferroelectricity, thermoelectricity, and topological state.

MATERIALS AND METHODS

Synthesis of 2D-AZnSb (A = Li, Na, and K) and 2D-ZnSb crystals

All manipulations for synthesizing samples were carried out in glove boxes filled with recirculating high-purity Ar (99.999%) to suppress oxygen and moisture concentrations below 0.1 parts per million because alkali metals are highly reactive under ambient conditions. The polycrystalline 3D-ZnSb pellet was prepared by the solid-state reaction of high-purity Zn powder and Sb shot at 600°C for 12 hours. The mixture of alkali metal (A = Li, Na, and K) and pulverized powders of 3D-ZnSb with the ratio of 1:1 was placed in an alumina crucible and then was sealed in an evacuated quartz tube under 10^{-3} Pa to avoid oxidization during the reaction. Polycrystalline 2D-AZnSb samples were synthesized by the solid-state reaction, where the sealed quartz tube with the alumina crucible was placed in a box furnace and annealed at 800°C for 24 hours. Then, the quartz tube was cooled to room temperature by turning off the heat. Single crystals of 2D-AZnSb samples were grown by self-flux method by using the alkali metal as a flux. After heating the sealed quartz tube containing the alumina crucible filled with the mixture of A and 3D-ZnSb at 800°C for 12 hours, the temperature slowly decreased down to 500°C for 100 hours. Then, the sample was cooled down to room temperature by turning off the power. We also synthesized the 2D-AZnSb by the solid-state reaction of each element. The mixture of A shot, Zn powder, and Sb shot with the ratio of 1:1:1 was prepared in glove boxes. The following procedures are the same as the synthesis of 2D-AZnSb using the mixture of A and 3D-ZnSb. The electrochemical reaction of 3D-ZnSb to 2D-LiZnSb was conducted by the discharge reaction in coin cell. The 2D-ZnSb samples were prepared by the selective etching of A ions by solution and electrochemical reactions. The etching by solution reaction was conducted in DI water–incorporated solutions for 2 to ~7 days. In the electrochemical reaction, the A ions were removed from the single crystalline 2D-AZnSb by the charge reaction at a current density of 10 μAh g^{-1} in coin cell. For the charge reaction, the coin cell was assembled in a glove box using a separator and an A foil as the reference electrodes, and 1 M $LiPF_6$ dissolved in 1:1 mixture of ethylene carbonate and diethyl carbonate solution was used as an electrolyte.

Structural and compositional analysis

The crystal structures of all 3D-ZnSb, 2D-AZnSb, and 2D-ZnSb samples were investigated by x-ray diffractometry (SmartLab, Rigaku) and probe-corrected scanning TEM (JEM-ARM200F, JEOL). We measured

the XRD patterns of all samples under high-quality Ar atmosphere using an atmosphere separator for SmartLab to prevent the oxidation during measurements. The TEM sample preparation was carried out using a dual-beam focused ion beam (FIB) (AURIGA CrossBeam Workstation, Carl Zeiss) slicing and lift-out technique. STEM-EDS and STEM–EELS (electron energy-loss spectroscopy) were used for the atomic scale–resolved chemical mapping and the lithium detection, respectively. The simulation of diffraction pattern was performed by using the CrystalMaker software with the parameters experimentally gained by XRD measurement. To prevent the oxidation of samples, an Ar-purged glove bag was attached to the entrance of FIB and TEM chambers during the loading and unloading processes. The chemical compositions of 3D-ZnSb, 2D-AZnSb, and A-etched 2D-ZnSb samples were analyzed by ICP-MS. The XPS of the samples was carried out using micro x-ray photoelectron spectrometer with a monochromatic Al Kα (1486.7 eV) x-ray source. The chamber pressure was maintained below 5.0×10^{-10} torr during the measurements. XPS spectra of single crystalline 2D-LiZnSb were obtained by cleaving in ultrahigh vacuum to prevent oxidation. XPS spectra of 3D-ZnSb and 2D-ZnSb were obtained after removing the surface contamination by using Ar gas cluster ion beam sputtering (*32*). To monitor any abnormality in the sample during the sputtering, a full survey spectrum and high-resolution XPS spectra measurements were made. The shift in the binding energy due to the relative surface charging was calibrated using the C 1s level at 284.6 eV as an internal standard.

In situ synchrotron XRD measurement of electrochemical reaction

For the analysis of the structural transformation, electrodes were prepared by mixing the 3D-ZnSb or 2D-ZnSb [70 weight % (wt %)] as an active material, super P (15 wt %) as a conductor, and polyvinylidene fluoride dissolved in *N*-methyl pyrrolidinone (15 wt %) as a binder on copper foil substrates. These materials were dried under vacuum at 80°C for 8 hours. The coin cell was assembled in a dry room. Electrochemical discharge-charge reactions of 3D-ZnSb and 2D-ZnSb were performed with a potential range between 3.0 to ~0.63 V (3D-ZnSb) and 3.0 to ~0.6 V (2D-ZnSb) at a current density of 100 mAh g^{-1}. In situ XRD measurement during the electrochemical reaction for 3D-ZnSb and 2D-ZnSb was carried out at the 5A beamline of the Pohang Accelerator Laboratory. The wavelength of the x-ray beam was 0.69265 Å, and XRD patterns were collected on a mar345 image plate detector in the transmission mode for every 3-min interval with 3 s of exposure time.

Characterization of electrical properties

All procedures for the measurement of electrical conductivity were carried out in glove boxes filled with high-purity Ar (99.999%). To measure the electrical properties of 2D-LiZnSb and 3D-ZnSb, electrical contacts in the six-point probe configuration were made with silver epoxy. Then, Apiezon N grease was coated onto the sample surfaces to prevent oxidation of samples during measurements. For 2D-ZnSb, we adopted the stamp method, where the 2D-ZnSb was cleaved by 3M Scotch tape and the exfoliated crystal was pressed with 3M Scotch tape onto the patterned electrodes on a SiO_2/Si wafer. The transferred sample was then pressed with a copper plate and firmly fixed.

Ab initio calculations

First-principles calculations based on density functional theory (DFT) were performed using generalized gradient approximation with the Perdew-Burke-Ernzerhof functional (*33*), as implemented in the Quantum Espresso package (*34*). The cutoff energy for the plane wave basis is set to 50 rydberg. The norm-conserving, optimized, designed nonlocal pseudopotentials were generated using Opium (*35*). The lattice parameters and atomic positions were fully relaxed until the pressures and forces are less than 10^{-2} kbar and 10^{-7} (in arbitrary units). For the *k*-point sampling from the Brillouin zone, the Monkhorst-Pack grids (8 by 8 by 8 and 8 by 8 by 1) (*36*) were used for the bulk and slab calculations, respectively. The interlayer binding energy was calculated from the total energy difference between bulk and isolated layers. To maintain the atomic structures of the layers, which are unstable, the unit cell and atomic positions were fixed for the binding energy calculations. The relativistic effect was fully considered by including spin-orbit coupling (SOC) in a noncolinear scheme. The DFT band structures and projected density of states (PDOS) of 3D-ZnSb, 2D-LiZnSb, and 2D-ZnSb were calculated including SOC. PDOS shows that the energy bands near the Fermi level mainly are composed of s- and p-orbitals of both Zn and Sb in all the three systems. Similarly, the contribution from the Li orbitals in 2D-LiZnSb is negligible in the band structure, as presented in fig. S9B. The energy bands of 3D-ZnSb and 2D-LiZnSb show that they are both semiconductors with an indirect gap of 0.05 and 0.29 eV for 3D-ZnSb and 2D-LiZnSb, respectively. These results are in good agreement with the previous first-principles band calculations (*22*, *37*). From the first-principles total energy calculations, the cohesive energy (ΔE_{coh}) is obtained by using

$$\Delta E_{coh} = [E_{ZnSb} - (E_{Zn} + E_{Sb})]/n_{ZnSb} \quad (1)$$

where E_{ZnSb}, E_{Zn}, and E_{Sb} are the total energies of ZnSb, Zn, and Sb, respectively, and n_{ZnSb} is the number of ZnSb per unit cell. The cohesive energies of 3D-ZnSb and 2D-ZnSb were calculated as –5.23 and – 4.65 eV per ZnSb, respectively. Although these results show that 3D-ZnSb is more stable, the cohesive energy of 2D-ZnSb is reasonably large enough, indicating that the 2D-ZnSb exists as a stable material, which can be synthesized in experiments. The Li alloying energy ($\Delta E_{Li\ alloying}$) can be obtained from

$$\Delta E_{Li\ alloying} = [E_{LiZnSb} - (E_{Li} + E_{ZnSb})]/n_{Li} \quad (2)$$

where E_{LiZnSb} and E_{Li} are the total energies of 2D-LiZnSb and Li, respectively, and n_{Li} is the number of Li per unit cell. With respect to the reference energies of 3D-ZnSb and 2D-ZnSb, the Li alloying energies for 3D-ZnSb and 2D-ZnSb were calculated as –2.19 and – 2.77 eV and per Li, inferring that Li-alloyed 2D-LiZnSb is energetically most stable. The interlayer binding energy (E_{inter}) of 2D-ZnSb was calculated in comparison to 3D-ZnSb (fig. S7). A unit cell of 2D-ZnSb comprises two distinct ZnSb layers; one has Sb atoms buckled upward, while the other has Sb atoms buckled downward with respect to the Zn atoms. A close inspection of the atomic structure reveals that there are two possibilities to separate the layers, enabling the calculations of two interlayer binding energies, which are indicated by the red dashed lines in fig. S7. To separate them, the Sb-Sb bonding should be broken in the red dashed line 3 case, while the interlayer Sb-Sb bonding should be broken for the red dashed line 4 case. The interlayer binding energies of 2D-ZnSb are calculated as 328 and 306 meV per atom for lines 3 and 4 cases, respectively. These values are definitely weaker than typical 3D primary bondings, thus concluding that the crystal structure of 2D-ZnSb presents a high anisotropy as a prominent aspect for layered materials. The bonding strengths at the red dashed lines in fig. S7 are

calculated as 872 and 697 meV per atom for lines 1 and 2 cases, respectively. Again, they near the chemical bonding regime, exhibiting the sp^3 nature of the bondings and the 3D nature of the material. Last, we calculated the exfoliation energy of 2D-ZnSb using the proposed method (*38*), as shown in fig. S7. We relaxed the structures of the isolated layer of 2D-ZnSb. Regardless of how the interlayer bonds are broken, we obtained the same stable structure after the structural relaxation of bilayer 2D-ZnSb, not monolayer 2D-ZnSb, indicating that the monolayer of 2D-ZnSb is not a stable form. The exfoliation energy calculation results in 183 meV per atom, which again indicates that the bilayer of 2D-ZnSb can be easily exfoliated from the layered 2D-ZnSb, as one can expect from the layered structure of 2D-ZnSb. From the binding energy calculation of 2D-ZnSb, one may imagine the monolayer of 2D-ZnSb. We obtained the relaxed crystal structures and electronic energy band structures of the monolayer of 2D-ZnSb (fig. S9). The crystal structure is presented in the inset of fig. S9D. We cannot obtain the relaxed structure of the planar monolayer structure. Before the relaxation of atomic position and cell parameter, the cohesive energy of monolayer is −3.46 eV per ZnSb (1.18 eV per ZnSb higher than that of 2D-ZnSb). Because of the large total energy difference from 3D-ZnSb and 2D-ZnSb phases, one can hardly imagine a freestanding monolayer. The bilayer ZnSb has a semiconducting band structure with an indirect bandgap of 0.27 eV.

SUPPLEMENTARY MATERIALS

Supplementary material for this article is available at http://advances.sciencemag.org/cgi/content/full/5/6/eaax0390/DC1

Fig. S1. Crystal structure and synthetic pathway of 2D-AZnSb.
Fig. S2. 2D layered ZnSb polymorphs by the selective etching of alkali metals.
Fig. S3. Lithium detection for 2D-LiZnSb and 2D-ZnSb.
Fig. S4. Exfoliated nanosheets of Li-etched 2D-ZnSb.
Fig. S5. Structural confirmation of 2D-LiZnSb and determined structure of 2D-ZnSb.
Fig. S6. Crystal structure of 2D-ZnSb.
Fig. S7. 2D layered behavior of 2D-ZnSb.
Fig. S8. Octet rule for ZnSb bidimensional polymorphs.
Fig. S9. Band structure and PDOS.
Fig. S10. Structural phase transformation from 3D-ZnSb to 2D-ZnSb.
References (*39*–*47*)

REFERENCES AND NOTES

1. M. Chhowalla, H. S. Shin, G. Eda, L.-J. Li, K. P. Loh, H. Zhang, The chemistry of two-dimensional layered transition metal dichalcogenide nanosheets. *Nat. Chem.* **5**, 263–275 (2013).
2. K. S. Burch, D. Mandrus, J.-G. Park, Magnetism in two-dimensional van der Waals materials. *Nature* **563**, 47–52 (2018).
3. C. Gong, X. Zhang, Two-dimensional magnetic crystals and emergent heterostructure devices. *Science* **363**, eaav4450 (2019).
4. B. Anasori, M. R. Lukatskaya, Y. Gogotsi, 2D metal carbides and nitrides (MXenes) for energy storage. *Nat. Rev. Mater.* **2**, 16098 (2017).
5. K. Watanabe, T. Taniguchi, H. Kanda, Direct-bandgap properties and evidence for ultraviolet lasing of hexagonal boron nitride single crystal. *Nat. Mater.* **3**, 404–409 (2004).
6. A. K. Geim, K. S. Novoselov, The rise of graphene. *Nat. Mater.* **6**, 183–191 (2007).
7. Y. Zhang, Y.-W. Tan, H. L. Stormer, P. Kim, Experimental observation of the quantum Hall effect and Berry's phase in graphene. *Nature* **438**, 201–204 (2005).
8. A. J. Mannix, B. Kiraly, M. C. Hersam, N. P. Guisinger, Synthesis and chemistry of elemental 2D materials. *Nat. Rev. Chem.* **1**, 0014 (2017).
9. J. N. Coleman, M. Lotya, A. O'Neill, S. D. Bergin, P. J. King, U. Khan, K. Young, A. Gaucher, S. De, R. J. Smith, I. V. Shvets, S. K. Arora, G. Stanton, H.-Y. Kim, K. Lee, G. T. Kim, G. S. Duesberg, T. Hallam, J. J. Boland, J. J. Wang, J. F. Donegan, J. C. Grunlan, G. Moriarty, A. Shmeliov, R. J. Nicholls, J. M. Perkins, E. M. Grieveson, K. Theuwissen, D. W. McComb, P. D. Nellist, V. Nicolosi, Two-dimensional nanosheets produced by liquid exfoliation of layered materials. *Science* **331**, 568–572 (2011).
10. V. Georgakilas, J. A. Perman, J. Tucek, R. Zboril, Broad family of carbon nanoallotropes: Classification, chemistry, and applications of fullerenes, carbon dots, nanotubes, graphene, nanodiamonds, and combined superstructures. *Chem. Rev.* **115**, 4744–4822 (2015).
11. P. F. McMillan, New materials from high-pressure experiments. *Nat. Mater.* **1**, 19–25 (2002).
12. D. H. Keum, S. Cho, J. H. Kim, D.-H. Choe, H.-J. Sung, M. Kan, H. Kang, J.-Y. Hwang, S. W. Kim, H. Yang, K. J. Chang, Y. H. Lee, Bandgap opening in few-layered monoclinic $MoTe_2$. *Nat. Phys.* **11**, 482–486 (2015).
13. Y. Qi, P. G. Naumov, M. N. Ali, C. R. Rajamathi, W. Schnelle, O. Barkalov, M. Hanfland, S.-C. Wu, C. Shekhar, Y. Sun, V. Süß, M. Schmidt, U. Schwarz, E. Pippel, P. Werner, R. Hillebrand, T. Förster, E. Kampert, S. Parkin, R. J. Cava, C. Felser, B. Yan, S. A. Medvedev, Superconductivity in Weyl semimetal candidate $MoTe_2$. *Nat. Commun.* **7**, 10038 (2016).
14. Y. Wang, J. Xiao, H. Zhu, Y. Li, Y. Alsaid, K. Y. Fong, Y. Zhou, S. Wang, W. Shi, Y. Wang, A. Zettl, E. J. Reed, X. Zhang, Structural phase transition in monolayer $MoTe_2$ driven by electrostatic doping. *Nature* **550**, 487–491 (2018).
15. H. Yang, S. W. Kim, M. Chhowalla, Y. H. Lee, Structural and quantum-state phase transitions in van der Waals layered materials. *Nat. Phys.* **13**, 931–937 (2017).
16. S. Cho, S. Kim, J. H. Kim, J. Zhao, J. Seok, D. H. Keum, J. Baik, D.-H. Choe, K. J. Chang, K. Suenaga, S. W. Kim, Y. H. Lee, H. Yang, Phase patterning for ohmic homojunction contact in $MoTe_2$. *Science* **349**, 625–628 (2015).
17. E. Kuramochi, M. Notomi, Phase-change memory. *Nat. Photon.* **9**, 712–714 (2015).
18. M. Acerce, D. Voiry, M. Chhowalla, Metallic 1I phase MoS2 nanosheets as supercapacitor electrode materials. *Nat. Nanotech.* **10**, 313–318 (2015).
19. G. A. Papoian, R. Hoffmann, Hypervalent bonding in one, two, and three dimensions: Extending the Zintl-Klemm concept to nonclassical electron-rich networks. *Angew. Chem. Int. Ed.* **39**, 2408–2448 (2000).
20. H.-J. Zhang, S. Chadov, L. Müchler, B. Yan, X.-L. Qi, J. Kübler, S.-C. Zhang, C. Felser, Topological insulators in ternary compounds with a honeycomb lattice. *Phys. Rev. Lett.* **106**, 156402 (2011).
21. P. J. Shaver, J. Blair, Thermal and electronic transport properties of *p*-type ZnSb. *Phys. Rev.* **141**, 649–663 (1966).
22. E. S. Toberer, A. F. May, C. J. Scanlon, G. J. Snyder, Thermoelectric properties of p-type LiZnSb: Assessment of ab initio calculation. *J. Appl. Phys.* **105**, 063701 (2009).
23. J. Wang, K. K. Manga, Q. Bao, K. P. Loh, High-yield synthesis of few-layer graphene flakes through electrochemical expansion of graphite in propylene carbonate electrolyte. *J. Am. Chem. Soc.* **133**, 888–8891 (2011).
24. C.-J. Shih, A. Vijayaraghavan, R. Krishnan, R. Sharma, J.-H. Han, M.-H. Ham, Z. Jin, S. Lin, G. L. C. Paulus, N. F. Reuel, Q. H. Wang, D. Blankschtein, M. S. Strano, Bi- and trilayer graphene solutions. *Nat. Nanotech.* **6**, 439–445 (2011).
25. L. Ding, Y. Wei, L. Li, T. Zhang, H. Wang, J. Xue, L.-X. Ding, S. Wang, J. Caro, Y. Gogotsi, MXene molecular sieving membranes for highly efficient gas separation. *Nat. Commun.* **9**, 155 (2018).
26. P. Liu, A. L. Cottrill, D. Kozawa, V. B. Koman, D. Parviz, A. T. Liu, J. Yang, T. Q. Tran, M. H. Wong, S. Wang, M. S. Strano, Emerging trends in 2D nanotechnology that are redefining our understanding of "nanocomposites". *Nano Today* **21**, 18–40 (2018).
27. K. E. Almin, The crystal structure of CdSb and ZnSb. *Acta Chem. Scand.* **2**, 400–407 (1948).
28. F. Winter, P. Pöttgen, M. Greiwe, T. Nilges, Lithium transition metal pnictides—Structural chemistry, electrochemistry, and function. *Rev. Inorg. Chem.* **35**, 11–24 (2015).
29. S. Yamanaka, M. Kajiyama, S. N. Sivakumar, H. Fukuoka, Preparation and single-crystal structure of a new high-pressure modification of $BaAl_2Si_2$. *Int. J. High Press. Res.* **24**, 481–490 (2004).
30. R. Demchyna, S. Leoni, H. Rosner, U. Schwaez, High-pressure crystal chemistry of binary intermetallic compounds. *Z. Cristallogr.* **221**, 420–434 (2006).
31. A. Nie, Y. Cheng, Y. Zhu, H. Asayesh-Ardakani, R. Tao, F. Mashayek, Y. Han, U. Schwingenschlögl, R. F. Klie, S. Vaddiraju, R. Shahbazian-Yassar, Lithiation-induced shuffling of atomic stacks. *Nano Lett.* **14**, 5301–5307 (2014).
32. T. Miyayama, N. Sanada, S. R. Bryan, J. S. Hammond, M. Suzuki, Removal of Ar^+ bean-induced damaged layers from polyimide surfaces with argon gas cluster ion beams. *Surf. Interface Anal.* **42**, 1453–1457 (2010).
33. J. P. Perdew, K. Burke, M. Ernzerhof, Generalized gradient approximation made simple. *Phys. Rev. Lett.* **77**, 3865–3868 (1996).
34. P. Giannozzi, S. Baroni, N. Bonini, M. Calandra, R. Car, C. Cavazzoni, D. Ceresoli, G. L. Chiarotti, M. Cococcioni, I. Dabo, A. D. Corso, S. Gironcoli, S. Fabris, G. Fratesi, R. Gebauer, U. Gerstmann, C. Gougoussis, A. Kokalj, M. Lazzeri, L. Martin-Samos, N. Marzari, F. Mauri, R. Mazzarello, S. Paolini, A. Pasquarello, L. Paulatto, C. Sbraccia, S. Scandolo, G. Sclauzero, A. P. Seitsonen, A. Smogunov, P. Umari, R. M. Wentzcovitch, Quantum espresso: A modular and open-source software project for quantum simulations of materials. *J. Phys. Condens. Matter* **21**, 395502 (2009).
35. A. M. Rappe, K. M. Rabe, E. Kaxiras, J. D. Joannopoulos, Optimized pseudopotentials. *Phys. Rev. B* **41**, 1227–1230 (1990).

36. H. J. Monkhorst, J. D. Pack, Special points for Brillouin-zone integrations. *Phys. Rev. B* **13**, 5188–5192 (1976).
37. K. Niedziolka, R. Pothin, F. Rouessac, R. M. Ayral, P. Jund, Theoretical and experimental search for ZnSb-based thermoelectric materials. *J. Phys. Condens. Matter* **26**, 365401 (2014).
38. J. H. Jung, C.-H. Park, J. Ihm, A rigorous method of calculating exfoliation energies from first principles. *Nano Lett.* **18**, 2759–2765 (2018).
39. S. S. Batsanov, Van der Waals radii of elements. *Inorg. Mater.* **37**, 871–885 (2001).
40. A. Bondi, Van der Waals volumes and radii. *J. Phys. Chem.* **68**, 441–451 (1964).
41. B. Cordero, V. Gómez, A. E. Platero-Prats, M. Revés, J. Echeverría, E. Cremades, F. Barragán, S. Alvarez, Covalent radii revisited. *Dalton Trans.* **21**, 2832–2838 (2008).
42. M. Ashton, J. Paul, S. B. Sinnott, R. G. Hennig, Topology-scaling identification of layered solids and stable exfoliated 2D materials. *Phys. Rev. Lett.* **118**, 106101 (2017).
43. P. Ares, F. Aguilar-Galindo, D. Rodríguez-San-Miguel, D. A. Aldave, S. Díaz-Tendero, M. Alcamí, F. Martín, J. Gómez-Herrero, F. Zamora, Mechanical isolation of highly stable antimonene under ambient conditions. *Adv. Mater.* **28**, 6332–6336 (2016).
44. X. Wu, Y. Shao, H. Liu, Z. Feng, Y.-L. Wang, J.-T. Sun, C. Liu, J.-O. Wang, Z.-L. Liu, S.-Y. Zhu, Y.-Q. Wang, S.-X. Du, Y.-G. Shi, K. Ibrahim, H.-J. Gao, Epitaxial growth and air-stability of monolayer antimonene on $PbTe_2$. *Adv. Mater.* **29**, 1605407 (2017).
45. W. B. Pearson, The crystal structures of semiconductor and a general valence rule. *Acta Crystallogr.* **17**, 1–15 (1964).
46. H. Schäfer, B. Eisenmann, W. Müller, Zintl phase: Transitions between metallic and ionic bonding. *Angew. Chem. Int. Ed.* **12**, 694–712 (1973).
47. E. Mooser, W. B. Pearson, Chemical bond in semiconductors. *Phys. Rev.* **101**, 1608–1609 (1956).

Acknowledgments

Funding: This work was supported by a National Research Foundation of Korea (NRF) grant funded by the Korean government (Ministry of Science, ICT and Future Planning) (no. 2015M3D1A1070639) and IBS-R011-D1. **Author contributions:** S.W.K. conceived the idea and organized the research. J.S. grew the single crystals and fabricated all the polycrystals. J.S. and H.Y.S. performed the chemical etching, and S.L. performed the electrochemical etching of 2D-LiZnSb. J.S., Z.W., and S.H.O. performed the TEM measurement. J.S. and S.W.K. analyzed the structure. J.S. and H.Y.S. performed the transport measurement. J.S., H.Y.S., J.-Y.H., K.H.L., and S.W.K. analyzed the electrical properties. J.S., S.Y.L., and J.L. performed the XPS measurement. J.S., S.Y.L., J.L., and S.W.K. analyzed the electron transfer. D.K., Y.K., and S.W.K. carried out the computational studies. J.S. performed the in situ XRD measurement. J.S. and S.W.K. analyzed the structural phase transformation. All authors discussed the results and contributed to writing the manuscript. **Competing interests:** The authors declare that they have no competing interests. **Data and materials availability:** All data needed to evaluate the conclusions in the paper are present in the paper and/or the Supplementary Materials. Additional data related to this paper may be requested from the authors. Correspondence and requests for materials should be addressed to S.W.K.

Submitted 16 February 2019
Accepted 17 May 2019
Published 28 June 2019
10.1126/sciadv.aax0390

Citation: J. Song, H. Y. Song, Z. Wang, S. Lee, J.-Y. Hwang, S. Y. Lee, J. Lee, D. Kim, K. H. Lee, Y. Kim, S. H. Oh, S. W. Kim, Creation of two-dimensional layered Zintl phase by dimensional manipulation of crystal structure. *Sci. Adv.* **5**, eaax0390 (2019).